Ways & Means

Zernike Phase Contrast Cryo-Electron Microscopy and Tomography for Structure Determination at Nanometer and Subnanometer Resolutions

Kazuyoshi Murata,[1,4] Xiangan Liu,[1,4] Radostin Danev,[2] Joanita Jakana,[1] Michael F. Schmid,[1] Jonathan King,[3] Kuniaki Nagayama,[2] and Wah Chiu[1,*]

[1]National Center for Macromolecular Imaging, Verna and Marrs Mclean Department of Biochemistry and Molecular Biology, Baylor College of Medicine, Houston, TX 77030, USA
[2]Okazaki Institute for Integrative Bioscience, National Institute of Natural Sciences, Okazaki, Aichi 444-8787, Japan
[3]Department of Biology, Massachusetts Institute of Technology, Cambridge, MA 02139, USA
[4]These authors contributed equally to this study
*Correspondence: wah@bcm.edu
DOI 10.1016/j.str.2010.06.006

SUMMARY

Zernike phase contrast cryo-electron microscopy (ZPC-cryoEM) is an emerging technique that is capable of producing higher image contrast than conventional cryoEM. By combining this technique with advanced image processing methods, we achieved subnanometer resolution for two biological specimens: 2D bacteriorhodopsin crystal and epsilon15 bacteriophage. For an asymmetric reconstruction of epsilon15 bacteriophage, ZPC-cryoEM can reduce the required amount of data by a factor of $\sim$3, compared with conventional cryoEM. The reconstruction was carried out to 13 Å resolution without the need to correct the contrast transfer function. New structural features at the portal vertex of the epsilon15 bacteriophage are revealed in this reconstruction. Using ZPC cryo-electron tomography (ZPC-cryoET), a similar level of data reduction and higher resolution structures of epsilon15 bacteriophage can be obtained relative to conventional cryoET. These results show quantitatively the benefits of ZPC-cryoEM and ZPC-cryoET for structural determinations of macromolecular machines at nanometer and subnanometer resolutions.

INTRODUCTION

In cryo-electron microscopy (cryoEM), biological specimens, such as purified proteins, virus particles, organelles and cells, are embedded in amorphous ice by rapid freezing (Dubochet et al., 1988; Baker et al., 2009) and are directly observed in the microscope while maintaining them at low temperature. The frozen, hydrated specimens can be considered as phase objects in transmission electron microscopy, and the 3D density function of their contents can be retrieved from the images (Toyoshima and Unwin, 1988).

In a conventional cryoEM, the image contrast of such phase objects is mainly generated by a combination of lens aberration and defocus (Scherzer, 1949). In frequency space, the data are modulated by the sinusoidal contrast transfer function (CTF) and are damped by exponential envelope functions, causing weak contrast at low frequency, loss of information at the nodes of the CTF, and a fall-off in signal at high frequency (Hanszen, 1971; Thon, 1971). Because of the electron optics and the low dosage used to record images of frozen hydrated biological specimens, the image contrast is generally low. The enhancement of signal-to-noise ratio (SNR) is achieved through extensive data processing by aligning and averaging multiple copies of identical objects. The lower the image contrast, the more difficult it is to align the images accurately. Therefore, low image contrast, especially at low resolution, is a major hurdle in structural determination of small biological objects.

Using the original idea proposed by Zernike (1942) to enhance the image contrast in a light microscope, two different approaches have been followed for transmission electron microscopy (Boersch, 1947). One method is to use an electrostatic field generated by an electrode inserted into the back-focal plane of the objective lens, which alters the phase of the unscattered beam that then interferes with the scattered beam to form the image. Recent microfabrication technology allows manufacturing of a micron-size device (Cambie et al., 2007; Majorovits et al., 2007; Schultheiss et al., 2006). However, the presence of the electrode produces a distorted image. The other method is to use a thin film made of carbon, with a central hole of submicron diameter as a phase plate. This thin film phase plate is also placed in the back-focal plane, with the unscattered beam going through the hole unchanged, and the phase of the diffracted beam shifted by $\pi/2$. The $\pi/2$ phase shift in the scattered beam changes the CTF from a sine to a cosine function (Nagayama, 2005) and thus substantially enhances the low-frequency contrast. Furthermore, the image can be taken at close to zero defocus so that there is no data loss due to the CTF nodes in the data. This approach has been attempted numerous times in the past without success (Badde and Reimer, 1970; Balossier and Bonnet, 1981; Faget et al., 1962; Johnson and Parsons, 1973; Kanaya et al., 1958; Krakow and Siegel, 1975; Parsons and Johnson, 1972; Unwin, 1970; Willasch, 1975). Only recently has contamination of the phase plate while inside the microscope been partially overcome, making this approach practical (Danev et al., 2009).
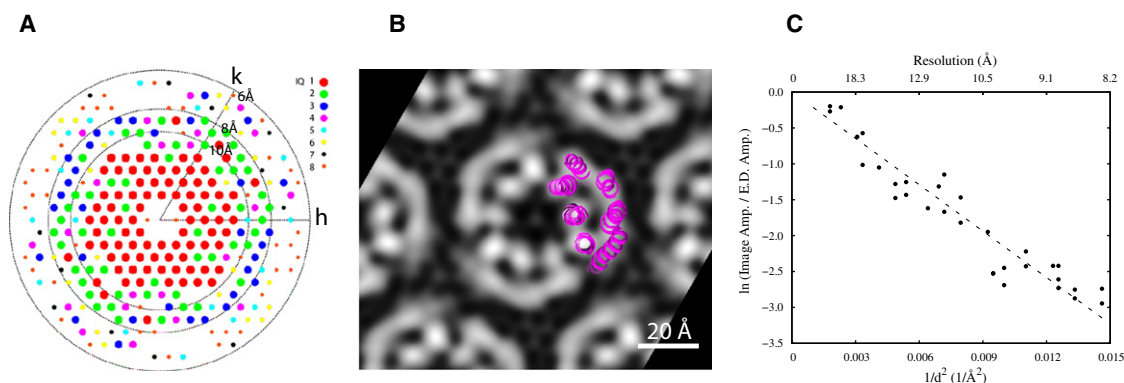
Figure 1. ZPC 2D Crystal Analysis of Bacteriorhodopsin

(A) IQ distribution of Fourier diffraction amplitudes calculated from a representative ZPC image of the 2D bacteriorhodopsin crystal. Different sizes of the dots with different colors indicate the S/N graded from IQ 1 to 8 for each diffraction spot. The IQ scale is based on Henderson's convention (Henderson et al., 1986) with 1 being the best. Dashed circles indicate resolution ranges of 10, 8, and 6 Å, respectively.

(B) Projection map of the 2D bacteriorhodopsin crystal to 8 Å resolution. The map was calculated from three crystal images by averaging and imposing P3 symmetry. A ribbon model of bacteriorhodopsin (PDB ID: 1BRD) is superimposed on the map.

(C) Plots of the ratio of computed diffraction amplitudes to electron diffraction amplitudes as a function of resolution. The computed diffraction amplitudes are extracted from the merged data set. The referenced electron diffraction amplitudes are taken from the published values (Henderson et al., 1986). A trend line is drawn based on the data points up to 8 Å, indicating the crystallographic B-factor to be ~860 Å^2. See also Figure S1 and Table S1.

Zernike phase contrast cryoEM (ZPC-cryoEM) has been used to image ice-embedded biological specimens, including proteins, viruses, and cells, at low and moderate resolutions (Yamaguchi et al., 2008). A single-particle reconstruction of a 14-fold symmetric GroEL has been obtained at 12 Å resolution (Danev and Nagayama, 2008). That study showed that the number of images was reduced by ~30% to get the same resolution, compared with a reconstruction from conventional images. Such data reduction is smaller than the theoretical expectation (Chang et al., 2010). In our current study, we combined a state-of-the-art electron cryomicroscope equipped with a C-film phase plate at the focal plane of the objective lens for data collection and data processing method for image reconstruction. We applied it to two well-known structures (2D bacteriorhodopsin crystals and epsilon15 bacteriophages) and were able to reconstruct the epsilon15 bacteriophage at better resolution with much fewer data than by using conventional images. New structural features were revealed from the asymmetric reconstruction of epsilon15 by this approach.

RESULTS

2D Crystal Analysis of Bacteriorhodopsin

Three ZPC-cryoEM images of trehalose-embedded bacteriorodopsin 2D crystals were collected at close-to-focus conditions on a 4 × 4 k CCD camera using a low-dose system. Each image contains ~19,000 unit cells. The image shows a characteristic crystal edge but not an obvious crystalline lattice (see Figure S1A available online). However, the computed Fourier transform of the image showed diffraction spots corresponding to the crystal lattice (Figure S1B). The CTF rings are difficult to discern until one computes a 1D power spectrum using the azimuthal average (Figure S1C), wherein we can only detect one CTF minimum in this example. We used the IQ plot (Hender-son et al., 1986) to evaluate SNR of the computed intensities of the diffraction spots from the crystal image. The SNR of a diffraction spot is graded by an IQ value ranging from 1 to 8 (1 for the best). Figure 1A shows an example of the IQ plot from a single image, in which the crystal lattice has been unbent to correct for the crystal distortion (Henderson et al., 1986). About 90% of the reflections out to 8 Å resolution have a ranking better than grade 4.

Ideally, the defocus value of an optimal ZPC image should be set close to zero defocus without CTF oscillation till reaching the Scherzer limit. However, our ZPC image still has a CTF oscillation, because it is hard to manually set the specimen focus precisely in the presence of the phase plate. The first CTF zeros (Figure S1C) of the three images were found to be between 11 and 9 Å by the *ctffind3* program (Mindell and Grigorieff, 2003). The projection map (Figure 1B) was reconstructed from the three merged images with P3 symmetry imposed after correcting crystal distortion and CTF in each image. The projection densities of the seven transmembrane α helices can be clearly seen in the resulting map.

After flipping the phases to correct for the CTFs of the three images, we evaluated the Fourier amplitudes and phases of the reconstructed projection map. The ratio of the image-derived amplitudes to the previously published electron diffraction amplitudes showed a linear decay to 8 Å (Figure 1C). The slope of the fitting line corresponds to a crystallographic *B* factor of about 860 Å^2. Furthermore, we compared the averaged phases of the diffraction spots from the three merged images with results from a previous study (Henderson et al., 1986). The average phase difference for all diffraction spots out to 8 Å was about 9.75 ± 8.11° and the average phase difference in the range 8 Å to 10 Å was less than 11.26° (Table S1). This result showed that structural information of bacteriorhodopsin was retrievable to 8 Å, which is sufficient to resolve secondary structure elements such as transmembrane α helices.
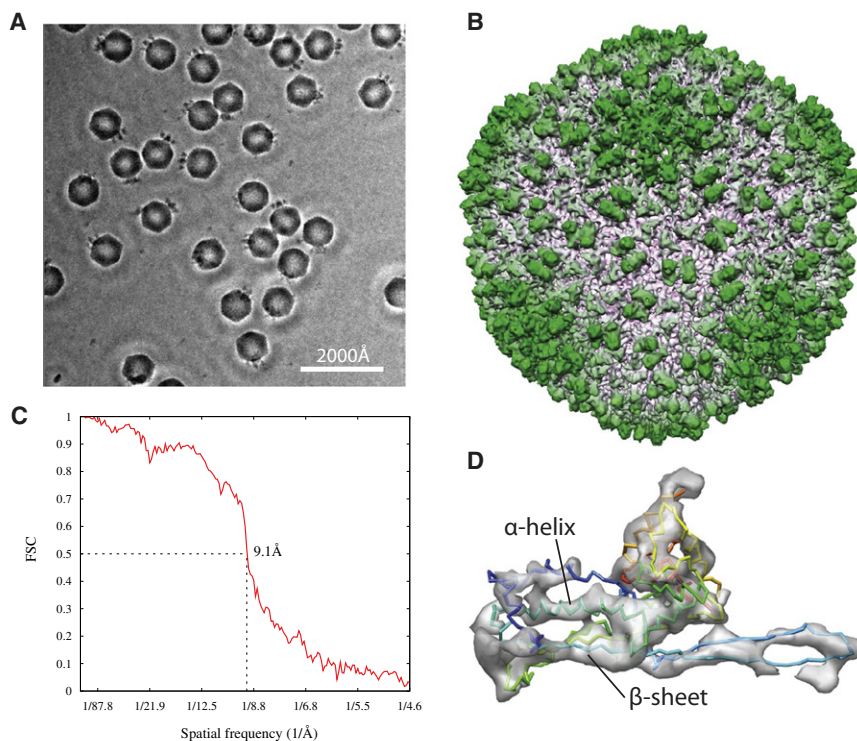
Figure 2. ZPC Single-Particle Reconstruction of Epsilon15 Bacteriophage with Icosahedral Symmetry Imposed

(A) Representative ZPC image of ice-embedded epsilon15 bacteriophage. Images were collected on CCD at a detector magnification of 75,000× aimed at a close-to-focus condition.

(B) Icosahedral reconstruction of epsilon15 bacteriophage; 2900 particles with no CTF phase flip to 1/9 Å^{-1} were selected and averaged after determining the alignment parameters.

(C) Fourier Shell Correlation (FSC) curve of the icosahedral map. The map resolution was estimated to be 9 Å according to 0.5 FSC between split datasets.

(D) Backbone model of gp7 is fitted into the corresponding capsid density. The map clearly visualizes a long α helix and a large β sheet. The backbone model verified the correctness of the reconstructed density. See also Figure S2.

Reconstruction of Epsilon15 Bacteriophage with Icosahedral Symmetry Imposed

ZPC-cryoEM images of ice-embedded epsilon15 bacteriophages show high contrast (Figure 2A), and the tail hub and surrounding tail spikes can be seen clearly. The halo surrounding a particle is due, in part, to the effect of the cut-on frequency of the phase plate hole (Danev et al., 2009). Using the Multi-Path Simulated Annealing (MPSA) refinement procedure (Liu et al., 2007), we reconstructed a 10 Å resolution icosahedral map without a CTF correction from 4,500 good particle images, which were selected from 6,188 raw particle images on the basis of the consistency criterion of MPSA. In contrast to the seven or eight iterations generally required by MPSA to refine a structure from scratch with conventional cryoEM images, the entire refinement process for ZPC-cryoEM images from a random model took only four iterations. The central slices of the maps in each of the four iterations (Figures S2A–S2E) show progressively improved structural features.

To extend the resolution beyond 10 Å, we expected that we would have to correct the CTF or eliminate some high-defocus particle images from the data set. However, the CTF rings were not apparent, compared with the case of the 2D crystal images (Figure S1B). We implemented a new method, cross-common-line correlation analysis (see Experimental Procedures), to determine the first CTF zero of each individual particle image. The correlation curve (Figure S2F) was calculated from the common lines between a raw particle image and the 2D references projected from the 10 Å density map, which was reconstructed from the 4500 particle images without making any CTF correction. When the correlation curve becomes negative, it presumably suggests that the CTF has passed the first CTF zero cross-

over (Figure S2F) and thus no longer agrees with the 10 Å model map. About 1600 particle images whose first CTF zeros fall below 1/10 Å^{-1} were removed from the reconstruction because of the uncertainty in determining the CTF zeros beyond the first one with confidence. Including only the remaining 2900 particle images without any CTF flip, we improved the map's resolution to 9 Å (Figures 2B and 2C). In this subnanometer resolution map, long α helices and large β sheets of the capsid subunits (gp7) can be visualized and match well with the established backbone model (PDB: 3C5B) (Jiang et al., 2008) (Figure 2D).

Reconstruction of Epsilon15 Bacteriophage with No Symmetry Imposed

We boxed out the same particles with a larger image size than that used for the icosahedral reconstruction in order to include the phage tail. We applied the orientations of the 5600 good particle images (from the third icosahedral iteration described above) to the corresponding large-box particle images. Using a newly developed asymmetric reconstruction procedure in MPSA (Liu et al., 2010b), we were able to reconstruct a 13 Å density map without imposing symmetry and without any CTF correction (Figure 3; Figure S3). This asymmetric reconstruction was done without using a known epsilon15 tail model, to eliminate model bias (Liu et al., 2010b). The capsomere features of the major protein (gp7) and the dimeric feature of the capsid stapling protein (gp10) were clearly visible in this 13 Å asymmetric density map as expected (Jiang et al., 2008).

The portal vertex complex, located at one of the 12 five-fold vertices, contains several proteins: tail hub, tail spikes, portal, and core proteins (Figures 3E–3H). This map reveals several new structural features that were not resolved in the previous 20 Å asymmetric reconstruction (Jiang et al., 2006). Figure 3A clearly shows that the tail hub has six subunits surrounded by the six tail spikes. The tail spike consists of two domains shaped like a bent arm (Figure 3E): the proximal stem domain
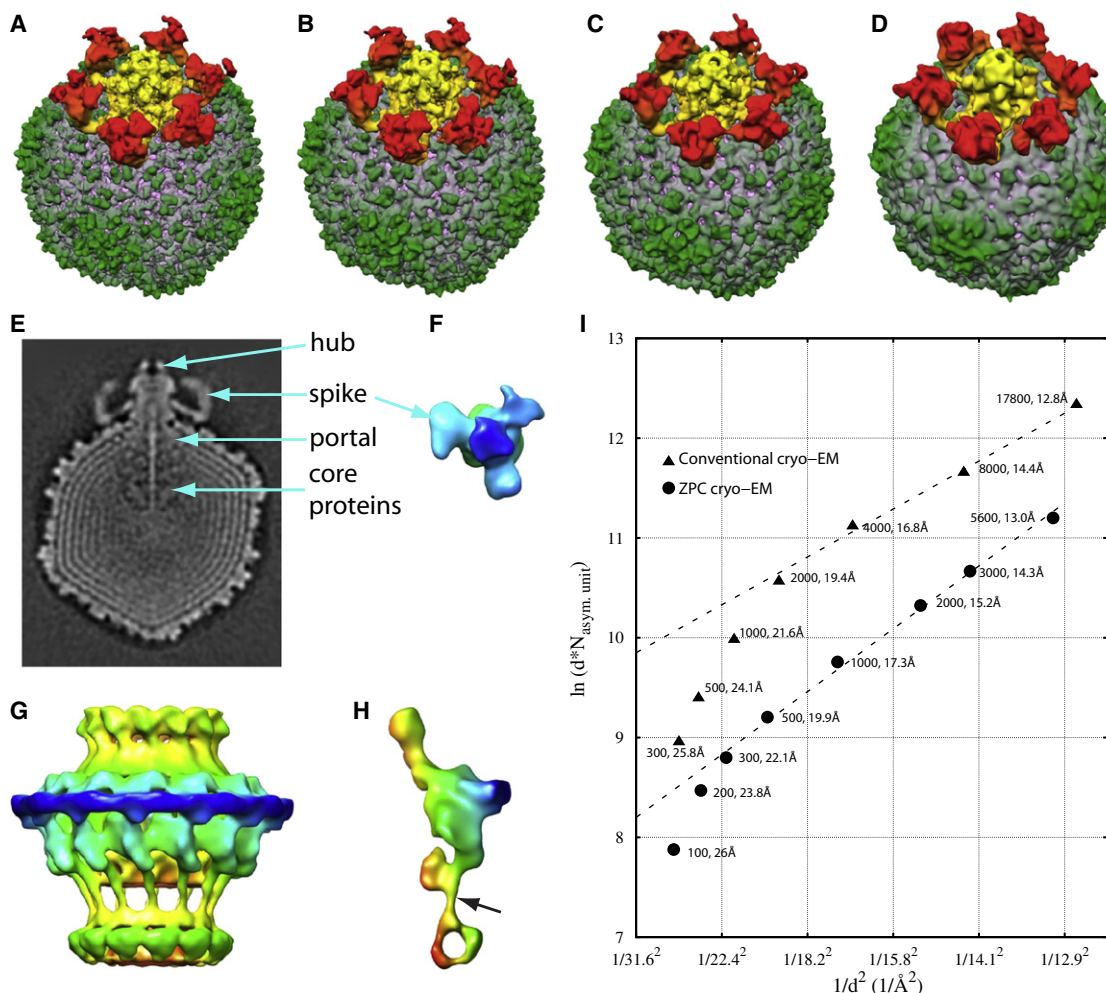
Figure 3. ZPC Single-Particle Reconstruction of Epsilon15 Bacteriophage with No Symmetry Imposed

(A) Asymmetric reconstruction of epsilon15 bacteriophage from 5600 particles without CTF correction. The map has 13 Å resolution according to 0.5 FSC criterion.

(B–D) Asymmetric reconstruction maps from sub-datasets with 1500, 500, and 100 particles. The 1500-particle map was directly reconstructed from the 1500 particles randomly picked from the last iteration of the 2000 particle sub-dataset.

(E) The central slice of the asymmetric map from (A). The portal vertex complex structures, core proteins and dsDNA are visible.

(F) The trimer structure of a tail-spike (gp20) from (A) viewed from 5-fold axis. The tail-spike was low-pass-filtered to emphasize the trimeric feature.

(G) The portal structure from (A) with 12-fold symmetry imposed.

(H) One subunit portal structure segmented (Pintilie et al., 2010) from (G). Arrow indicates a long helix that has been found in the portal structure of cyanophage P-SSP7 (Liu et al., 2010a).

(I) "Crystallographic" *B* factors of the single particle images. The triangle symbols represent the structures reconstructed from conventional cryoEM images. The dots represent the reconstructions from ZPC-cryoEM images. The number of particles and the corresponding resolution are marked nearby each data point. All the reconstructions were done independently from a random initial model. The *B* factors are 960 and 1200 Å² with respect to conventional and ZPC-cryoEM, which are equal to twice the slope of the fitted dashed lines. See also Figures S3 and S4.

is connected to the tail hub, and the distal flowerlike domain is connected by an elbow. Figure 3F shows that the low-pass-filtered tail spike has trimeric features viewed from the top. In fact, the entire flower-like domain is clearly split into three subunits, a feature that was not observed previously (Jiang et al., 2006).

Because it was shown previously that the portal protein has a 12-fold symmetry (Jiang et al., 2006), we applied a 12-fold symmetry to the portal density (Figure 3G). Its subunit structure is topologically similar to the 9 Å map of the cyanophage P-SSP7 (Liu et al., 2010a). The long "leg" density seen in the portal subunit (arrow in Figure 3H) appears to be analogous to the

Q-rich motif helix near the C-terminal end of the P-SSP7 portal protein, which may play a role in the DNA release during phage infection.

Estimation of the "Crystallographic" *B* factor from Sub-Datasets in the Asymmetric Reconstruction
According the theoretical formula by Rosenthal and Henderson (2003),

$$N_{asym\ unit} = \left[\langle S \rangle^2 / \langle N \rangle^2 \bullet 30\pi/N_e \sigma_e d \right] \bullet e^{B/2d^2},$$

which shows the relationship between resolution (d), number of asymmetric units ($N_{asym\ unit}$), criterion for the SNR on amplitudes ($\langle S \rangle^2 / \langle N \rangle^2$), electron dose ($N_e$), electron scattering cross-section (σ_e), and crystallographic B factor of the data set, the B factor can be estimated from the slope of the curve of the number of asymmetric units versus resolution in different independent reconstructions (i.e., $B = 2 \bullet \Delta(\ln(Nd))/\Delta(1/d^2)$); here, Δ stands for the difference of the variable.

We generated seven subsets of data containing 3000, 2000, 1000, 500, 300, 200, and 100 particles, randomly selected from the entire raw single particle image dataset. Following the same asymmetric reconstruction procedures as above, we reconstructed asymmetric maps for each sub-dataset. Surprisingly, after four iterations of refinement, all seven sub-datasets had converged to their final icosahedral reconstructions from a random initial model. For conventional image data, we generally required over seven iterations before a converged map can be reached. For the asymmetric reconstruction, except for the 100-particle dataset, each of the datasets took only four more iterations to converge from an initial model generated from the icosahedral reconstruction (Liu et al., 2010a). Very unexpectedly, we were able to reconstruct a 26 Å map using only 100 particle images, without imposing any symmetry. Because a random model was used as the initial model for each reconstruction, no model bias was introduced (Liu et al., 2007). Typical reconstructions are shown in Figures 3B–3D. We plotted the relationship (Figure 3I) between the number of asymmetric units and the resolution of the map from all eight independent asymmetric reconstructions. From the slope of the curve in Figure 3I, we estimated the "crystallographic" B factor (Rosenthal and Henderson, 2003) of the particle images to be 1200 Å^2. In such an estimate, it is important to use an unbiased initial template for each refinement, as was done here.

Cryo-Electron Tomography of Epsilon15 Bacteriophages

An alternative method to obtain an asymmetric structure is to use cryo-electron tomography. The tilt series of the ice-embedded epsilon15 bacteriophage recorded in the ZPC electron microscope showed high-contrast images with a varying ripple around the particles (and all the other features of the images) derived from the cut-on frequency of the phase plate hole. The tomographic reconstruction directly delineated structural details of the individual bacteriophage (Figure 4A; Movie S1). We extracted 132 epsilon15 subtomograms from a single tomogram. We made sub-datasets with various numbers of subtomograms randomly selected from the total 132 subtomograms. For each sub-dataset, we used the *tomohunter* program (Schmid and Booth, 2008) to align the subtomograms in 3D space and then averaged them with and without icosahedral symmetry. To avoid model bias while aligning the subtomograms, we did not use any known model as a reference. The resolutions of all the sub-datasets using the 0.5 FSC criterion are illustrated in Figures 4B and 4C. It is noted that resolution of the averaged maps in either case (asymmetric and icosahedral) using the ZPC-cryoET data is not much improved when more than 50 subtomograms were used. The averaged map without any enforced symmetry clearly exhibited the features of the tail and the capsid shell (Figure 4D). The dimeric nature of the minor capsid protein, gp10, became
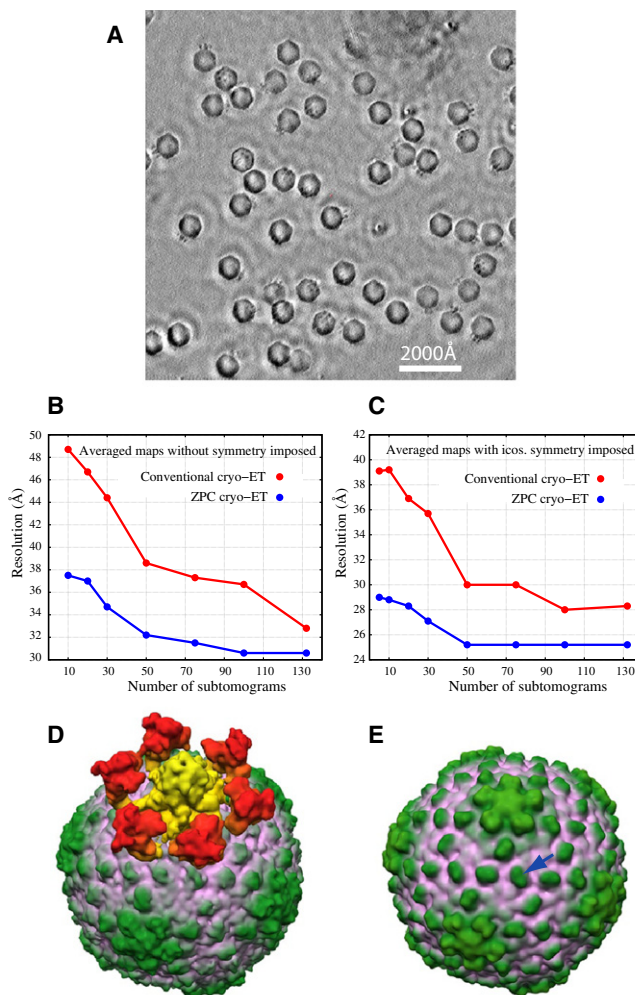
Figure 4. ZPC Cryo-ET and Subtomogram Averaging of Epsilon15 Bacteriophages

(A) The central slice of the reconstructed ZPC-cryoET tomogram of ice-embedded epsilon15 bacteriophages.

(B and C) The resolution curves of both conventional and ZPC cryoET are shown for asymmetric averages without symmetry imposed (B) and with icosahedral symmetry imposed (C). Each sub-dataset was independently aligned from a computer-generated icosahedral solid model from different sub-datasets randomly picked from the entire set of 132 subtomograms. The resolution improvement slows down for sub-datasets containing more than 50 subtomograms.

(D and E) The averaged asymmetric and icosahedral-imposed density maps from 50 subtomograms. The heterogeneity among the six tail-spikes can be clearly seen in the asymmetric map. The icosahedral-imposed map clearly shows the dimeric feature (arrow) of the capsid stapling protein (gp10). See also Movie S1.

visible in the icosahedral symmetry imposed map after the subtomogram averaging (arrow in Figure 4E).

Reconstruction Resolution Versus Particle Image Numbers in Conventional CryoEM

To assess the effects of ZPC-cryoEM on the numbers of particles needed to reconstruct the structure at a given resolution, we used the same instrument to collect conventional images of

ice-embedded epsilon15 bacteriophage particles and used the same software and procedures to perform both single particle and tomographic reconstructions. In either case, it is consistently found that the numbers of particles required for the same resolution reconstructions are reduced by a factor of ~3 for ZPC relative to the conventional images (Figure 3I and Figures 4B and 4C).

DISCUSSION

The theoretical advantages of ZPC-cryoEM are manifold, as previously enumerated (Nagayama, 2005). The study using GroEL as a test specimen showed the fidelity of the reconstruction to 12 Å from ZPC electron images (Danev and Nagayama, 2008). Our studies demonstrate practically attainable structures with images collected from the state-of-the-art Zernike phase contrast electron cryomicroscope and also reveal previously unseen structural features in a large virus, using fewer particle images than those from the conventional method.

CTF/Defocus Issues in Subnanometer Reconstructions Using ZPC-cryoEM

For ZPC imaging, the optimal defocus is always intended to be close to zero. However, it is hard to achieve this in practice. In our experiment, the defocus was manually adjusted using the live FFT function of the CCD camera control software. The CTF rings are barely visible at low defocus. As an alternative method, we tried to estimate the in-focus from a high defocus setting, where the CTF rings are more readily visible. However, this did not work because the hysteresis of the objective lens makes it difficult to return to the intended defocus. Therefore, it is very difficult to routinely and reliably obtain an image of a specimen in-focus with the current ZPC-cryoEM setting. Presently, to reconstruct a high-resolution map using ZPC, it is necessary to either correct the CTF for each image, as done with bacteriorhodopsin, or discard the "bad" defocus images computationally, as done with epsilon15 bacteriophage.

The bacteriorhodopsin 2D crystal offers an ideal specimen to assess the reliability of the reconstruction obtained from the ZPC images because its amplitudes and phases are known (Henderson et al., 1986). Among the three images of bacteriorhodopsin analyzed, there is no need to flip the CTF phases up to $1/11$ Å^{-1}. Beyond that, we had to determine the CTF parameters of the image, and the first zero of the CTF ring is barely visible (Figure S1C). However, the accuracy of the phases determined in our study gives a direct verification of its accuracy for 2D reconstruction up to 8 Å resolution (Table S1).

In the case of single-particle ZPC-cryoEM images, the CTF rings of the power spectrum of the summed particle images are not obvious. There exists no algorithm that can determine the CTF parameters of each individual particle in the absence of visible CTF rings when the particle structure is not known. Our method of using a cross-common-line correlation curve (Figure S2F; Experimental Procedures) is used to detect the position of the first CTF zero. Instead of correcting the CTF of the images, we used this information to remove the particle images whose first CTF zero falls below that spatial frequency. To find the correlation curve of a raw image, we used the 10 Å map as

a reference, which is the best map that can be reconstructed without considering the CTF; thus, we were able to eliminate images whose first CTF zero is at $1/10$ Å^{-1} or lower frequency. The resolution of the map generated from the selected particle images was then improved to ~9 Å. The fact that a subnanometer resolution single-particle structure can be obtained from the ZPC-cryoEM is fairly encouraging, because the structure at this resolution can reveal long α helices and a large β sheet (Figures 1C and 2D). Such structural features ensure the reliability of the reconstruction and allow the fitting of the density to the known structures of the molecular components with a higher level of confidence. The ability to achieve subnanometer resolution, combined with the enhancement of image contrast of ZPC-cryoEM, leads to the hope that subnanometer resolution is also possible for smaller proteins (<100 kDa) or small protein components in a large macromolecular assembly whose contrast is too low to detect in conventional cryoEM (Danev et al., 2009; Henderson, 1995).

Limiting Factors in Subnanometer Resolution Reconstructions for ZPC-CryoEM

To address the question of why the reconstructions of bacteriorhodopsin and epsilon15 were limited to ~8–9 Å, we evaluated the crystallographic B factor in both cases. For bacteriorhodopsin, we could determine this factor by comparing the known electron diffraction amplitude to our computed diffraction amplitude from the images (Henderson et al., 1986). In the case of epsilon15 bacteriophage, we did multiple reconstructions with different numbers of particles and determined their resolutions. The slope of the curve between number of particle images and resolution produced the crystallographic B factor using a theoretical formula (Rosenthal and Henderson, 2003). Using these methods, the crystallographic B factors were estimated to be ~860 and ~1200 Å^2 for bacteriorhodopsin 2D crystal and the single particle epsilon15 bacteriophage images respectively. Such B-factor values would limit the structural determination beyond the current resolution in the reconstruction (Henderson et al., 1986; Liu et al., 2007).

The determined crystallographic B factors in both cases are larger than that one would normally observe in conventional cryoEM reconstructions. In this study, we used a Tietz 4 × 4 k CCD camera as a recording medium because emulsion film was thought to generate contaminants in the microscope that would shorten the lifetime of a phase plate. The ZPC images of 2D crystals and single particles were recorded at 75,000× detector magnification (1.95 Å per pixel). The retrievable resolutions for typical reconstructions are expected to be between 2/5 and 2/3 Nyquist resolution depending on the type of CCD camera (Booth et al., 2004; Chen et al., 2008). Therefore, the modulation transfer function of the CCD camera could have been a source of resolution limitation in this case. However, the following independent experimental results indicate that the CCD camera is not a limiting factor in the current 8–9 Å resolution limit. The first experiment was the failure to improve the resolution of the 2D reconstruction of bacteriorhodopsin even with images taken at a higher magnification. The second experiment was based on visibility of the CTF ripples beyond 8 Å resolution from the conventional CCD images of epsilon15 bacteriophages taken at the same magnification (Figure S4).

Furthermore, from two independent sets of experiments, we found that the crystallographic *B* factors of ZPC-cryoEM images are larger than those of conventional images recorded by the same CCD camera in the same microscope. We first estimated the *B* factors from the fall-off of the CTF rings, calculated from images of an amorphous carbon film (Saad et al., 2001). The *B* factor of the phase plate data taken near zero defocus is ~30% higher than that of the conventional images taken at 1–2 μm defocus (data not shown). We alternatively obtained the *B* factors from multiple independent reconstructions of epsilon15 bacteriophage with different number of particles (Henderson et al., 1986; Liu et al., 2007). As shown in Figure 3I, the crystallographic *B* factor of images using the phase plate is ~20% higher than those without a phase plate. This shows the current limitation of phase plate technology and highlights the need for improvement. Possible causes for the relatively high *B* factor in ZPC images include charging (Danev et al., 2009) and variability in film thickness of the phase plate.

ZPC-CryoEM for Reconstruction Without Imposed Symmetry

There are two factors that affect the resolution of an asymmetric reconstruction—the accuracy of the determined asymmetric orientations and the number of raw particle images. ZPC-cryoEM could help with both these factors. Because there is no loss of structural information due to the CTF oscillation in the ZPC-cryoEM images, it is anticipated that ZPC-cryoEM will require fewer images than conventional images to ensure full data coverage in Fourier space for image reconstruction. In addition, the high image contrast allows easier and more accurate particle orientation determination. To evaluate fairly the reduction in the amount of data required for single particle 3D reconstruction, we collected epsilon15 data using the same electron microscope and CCD camera with and without a phase plate and processed the images with the same refinement programs. However, in contrast to the in-focus imaging of ZPC-cryoEM, we had to collect the conventional (without phase plate) images at a defocus ranging from 1 to 3 μm, which is the normal defocus range for conventional cryoEM. Figure 3I clearly shows that ZPC-cryoEM requires ~3-fold fewer data for the same resolution of the single-particle reconstruction over a broad range of resolutions, compared with the conventional cryoEM. In addition to requiring less data, Figures 3E–3H demonstrate convincingly that several of the structural features of the portal vertex complex of epsilon15 are better resolved than the ones in previous cryoEM asymmetric reconstruction with conventional images (Jiang et al., 2006).

Even though it is still technically tedious to obtain images with the current phase plate technology, a moderate resolution (9–30 Å) can provide very valuable structural information for understanding a complex macromolecular machine, which can be achieved without correcting CTF. Eliminating the need for correcting CTF will remove a huge technical barrier in using cryoEM as a routine structural tool.

Benefits of ZPC-CryoET

CryoET is a method that generates a low-resolution map from a single specimen. Therefore, the highly visible contrast of ZPC-cryo-ET would help to retrieve features from such data. In this study, we used epsilon15 bacteriophage as a test specimen because of its known structure. To find out by how much the SNR of ZPC-cryoET reconstructions can be enhanced, we averaged 132 subtomograms extracted from a single tomogram reconstruction. We also processed different sub-datasets with different numbers of subtomograms randomly chosen from the 132 subtomograms. Figures 4D and 4E show that using only 50 subtomograms can yield an average density map with features including major capsid shell, capsid stapling proteins, and all the molecular components of the portal vertex complex. The high structural similarity to that from the single-particle reconstruction validates the power of this approach. When we compared the resolution versus number of subtomograms averaged (Figures 4B and 4C), the resolution improvement slows down with 50 or more subtomograms. This phenomenon may be explained as the CTF effects starting to become significant in this set of data. However, the CTF starts to take effect at lower resolution in the conventional cryoET because of the large defocusing required for increasing the contrast. Therefore, the ZPC-cryoET offers obvious advantages for obtaining low-resolution structures without requiring CTF corrections. Nevertheless, it is likely that we will need to make such corrections for reconstruction beyond 20 Å because of the defocus gradient in the tilted specimens. Without correcting the CTF, 10 subtomograms of ZPC-cryoET generated an averaged map at 38 Å resolution, which can only be obtained by using more than 50 subtomograms from conventional cryoET. Therefore, a potential application of ZPC-cryoET is for cells and organelles where there may be no possibility of averaging identical objects to boost the SNR as shown here with the bacteriophage. The enhanced contrast in ZPC-cryoET may reveal some subcellular components without post-tomographic averaging which cannot be seen using conventional cryoET (Danev et al., 2010). Our study has demonstrated that ZPC-cryoEM and cryoET have the potential to carry this imaging modality into the next era of research, by bridging cellular and molecular structure at an unprecedented level of resolution.

EXPERIMENTAL PROCEDURES

Sample Preparation

2D bacteriorhodopsin crystals were prepared from *Halobacterium salinarum* S9 and were fused with octylglucoside and dodecyl trimethylammonium to make larger crystals (Baldwin and Henderson, 1984). The 2D crystals were embedded in 3% trehalose on a thin carbon film supported by a 300-mesh copper grid (Glaeser and Downing, 1990; Hirai et al., 1999). The sample grid was quickly frozen in liquid nitrogen before it completely dried and was stored in a cryo-storage tank.

Epsilon15 bacteriophage particles were purified from infected *Salmonella anatum* bacterial culture using sucrose gradient centrifugation, as described elsewhere (Jiang et al., 2006). R 1.2/1.3 Quantifoil grids (Quantifoil Micro Tools GmbH) chemically cleaned with acetone beforehand, were glow discharged for 10 s, and were covered with a thin layer of carbon support film. Three microliters of epsilon15 bacteriophage suspension was applied onto the Quantifoil grid, blotted with Whatman 1 filter paper at 95% humidity and room temperature, and quickly frozen in liquid ethane cooled by liquid nitrogen using a Vitrobot (FEI Company). For cryo-ET, 150 Å gold fiducial markers (Electron Microscopy Sciences) were added in the sample aliquot at 10% of the total volume before freezing. The frozen grids were stored in a liquid nitrogen cryo-storage tank.

Image Acquisition of Bacteriorhodopsin Crystals and Epsilon15 Bacteriophages

The frozen, hydrated grids were loaded onto a Gatan cryoholder (model 914, Gatan Inc.) and were imaged with a JEM2200FS electron microscope (JEOL Inc.) at liquid nitrogen specimen temperature. The instrument used in the present studies was a 200 kV electron microscope with a field emission gun, an in-column energy filter, and a turbo molecular pump. A Zernike phase plate, which consists of ~240 Å thick amorphous carbon film with a central 0.5 μm pinhole, was mounted on each hole of the 5 × 5 array aperture disc (Danev et al., 2009). Four aperture discs were simultaneously mounted on the special aperture holder implemented with a ceramic heater and were sustained in the back-focal plane of the objective lens. The discs were kept at 200°C at all times to avoid contamination. The ZPC-cryoEM images were recorded on a Tietz 4 × 4 k SlowScan CCD camera (15 μm pixel size) cooled to −25°C (TVIPS).

The ZPC images of the 2D bacteriorhodopsin crystal were collected with a dose rate of 20 electrons per Å^2 with a 1-second exposure time at nominal detector magnifications of 75,000× and 120,000× on the CCD, respectively. Focus was adjusted on a carbon film area adjacent to the recording position so that the CTF ring's first node extends to the highest frequency, using the live computed Fourier transform (live FFT).

The ZPC-cryoEM images of epsilon15 bacteriophage were collected with a detector magnification of 75,000× with the same instrument as for bacteriorhodopsin crystal. A total of 6188 particles were picked manually from 473 CCD frames using the EMAN *boxer* program (Ludtke et al., 1999). The same 6188 particles were used for both icosahedral and asymmetric reconstructions with image sizes of 450 × 450 and 576 × 576, respectively.

Image Processing of Bacteriorhodopsin Crystals

The 2D crystal images were processed by 2 dx software (Gipson et al., 2007a; Gipson et al., 2007b). First, we unbent the 2D crystal images three times, using different peak mask sizes and reference areas. On the basis of the unbent images, we determined and corrected CTF for each image using the *ctffind3* program implemented in the software. Three of 15 images showing the lowest phase residuals were selected for generating a projection map. The Fourier components of the three images were merged by refining the phase origins. In the final projection map, P3 symmetry was imposed. The merged amplitudes from the images were compared with the electron diffraction amplitudes (Henderson et al., 1986) and were plotted against the squared spatial frequency. The crystallographic *B* factor was estimated from the slope of the fitting line (Figure 1C).

Single-Particle Reconstruction of Epsilon15 Bacteriophage with and Without Symmetry Imposition

For icosahedral reconstruction, the alignment parameters of each particle image were determined by a Multi-Path Simulated Annealing optimization algorithm (MPSA) (Liu et al., 2007) based on cross common lines, and 3D synthesis was performed using the EMAN *make3d* program (Ludtke et al., 1999). Using the MPSA procedure, a small number of particles were assigned random orientations, from which an initial model was built and then iteratively refined. Finally, without any CTF assessment, 4558 good particles were selected using the consistency criterion of MPSA, resulting in a 10 Å resolution icosahedral map. For the asymmetric reconstruction, the asymmetric orientation was determined using cross common line between the tail image masked from a raw particle image and tail 2D references projected from a 3D tail model, as described elsewhere (Liu et al., 2010b).

To detect and remove high defocus particle images, which have their first CTF zero below 1/10 Å^{-1}, we used a cross common line correlation curve between each raw image and 12 references projected from the 10 Å map. Each point of the resulting correlation curve is the 10 pixel running average of the cosine of the phase residual for that resolution range using all the cross common lines. In the correlation curve, high defocus images showing a negative correlation within 10 Å were discarded. The remaining 2900 particle images were used to reconstruct the final 9 Å map. Resolution of the reconstruction was assessed according to 0.5 FSC between the two independently split datasets.

The structure factors of the final maps computed with or without symmetry imposition were rescaled to a synthetic 1-D structural factor that was generated through a procedure described in EMAN wiki (http://blake.bcm.tmc. edu/emanwiki/EMAN1/FAQ/StructureFactor) (Liu et al., 2010a). This structure factor rescaling has two functions: first, it boosts up high frequency signal to make the high-resolution features more visible, and second, it boosts up the very low frequency (lower than the cut-on frequency) signals that were suppressed as a result of the presence of the phase plate hole. The rescaled map was then low-pass-filtered at a frequency slightly higher than the nominal resolution of the reconstruction.

Cryo-ET Data Collection and Processing of Epsilon15 Bacteriophage

For ZPC-cryoET, tilt series of ice-embedded epsilon15 bacteriophage were collected with a Gatan 914 cryo-specimen holder at an angular increment of 2° with ± 70° specimen tilt and at a detector magnification of ~30,000× on CCD. The total accumulated dose was ~80 electrons per Å^2 using semiautomated low-dose tilt-series acquisition software (Danev et al., 2010).

Tomographic reconstruction was performed using IMOD software (Kremer et al., 1996). Fiducial gold markers (150 Å) included with the ice-embedded specimen were used for image alignment. Subtomograms of viral particles were extracted from the reconstructed tomogram. The alignment was done in two steps. First, the 20 Å low-pass-filtered subtomograms, in which the particle tails were excluded by a tight spherical mask, were iteratively aligned to the total average in each step using *tomohunter* program (Schmid and Booth, 2008) after initially being aligned to a computer-generated icosahedral model. Second, the tail density clearly visible at one of 12 five-fold vertices was manually oriented to the Z-axis. The tail of epsilon 15 bacteriophage has pseudo six-fold symmetry and is located at one of the five-fold vertices. To find the unique azimuthal orientation of the tail from the five orientation choices, we masked the tail, applied six-fold symmetry, and compared this symmetrized map with the single particle asymmetric map (Figure 3A) in 72° (five-fold) steps. The aligned subtomograms were averaged in reciprocal space by weighting the missing wedge to reduce orientation bias (Schmid and Booth, 2008). Resolutions of the asymmetric and icosahedrally averaged maps were assessed by comparing them with the higher-resolution single particle maps as described above, respectively.

Map Visualization

The visualization was done by UCSF Chimera (Pettersen et al., 2004). Amira was used for segmentation (Visage Imaging, Inc.). The backbone model of gp7 (PDB: 3C5B) was used to evaluate the segmented densities in the icosahedral map reconstructed by single-particle analysis.

ACCESSION NUMBERS

The density maps of epsilon15 bacteriophage obtained by single-particle or tomographic reconstructions have been deposited to the EMDB under accession numbers EMD-5206 (9 Å icosahedral reconstruction using 2900 ZPC-cryoEM particles), EMD-5207 (13 Å asymmetric reconstruction using 5600 ZPC-cryoEM particles), EMD-5208 (26 Å asymmetric reconstruction using 100 ZPC-cryoEM particles), EMD-5209 (13 Å asymmetric reconstruction using 17,800 conventional cryoEM particles), EMD-5203(32 Å ZPC tomographic reconstruction averaged from 50 subtomograms without imposing symmetry), and EMD-5204 (38 Å conventional tomographic reconstruction averaged from 50 subtomograms without imposing symmetry).

SUPPLEMENTAL INFORMATION

Supplemental Information includes four figures, one table, and one movie, and can be found with this article online at doi:10.1016/j.str.2010.06.006.

ACKNOWLEDGMENTS

REFERENCES

Badde, H.G., and Reimer, L. (1970). Der Einflus einer streuenden Phasenplatte auf das elektronen mikroskopische Bild. Z. Naturforschg. 25a, 760–765.

Baker, M.L., Marsh, M.P., and Chiu, W. (2009). Cryo-EM of molecular nanomachines and cells. In Nanotechnology, Vol. 5, V. Vogel, ed. (Weinheim, Germany: Wiley-VCH), pp. 91–111.

Baldwin, J., and Henderson, R. (1984). Measurement and evaluation of electron diffraction patterns from two-dimensional crystals. Ultramicroscopy 14, 319–335.

Balossier, G., and Bonnet, N. (1981). Use of electrostatic phase plate in TEM. Transmission electron microscopy: improvement of phase and topographical contrast. Optik (Stuttg.) 58, 361–376.

Boersch, H. (1947). Über die Kontraste von Atomen im Elektronenmikroskop. Z. Naturforsch. A 29, 615–633.

Booth, C.R., Jiang, W., Baker, M.L., Zhou, Z.H., Ludtke, S.J., and Chiu, W. (2004). A 9 angstroms single particle reconstruction from CCD captured images on a 200 kV electron cryomicroscope. J. Struct. Biol. 147, 116–127.

Cambie, R., Downing, K.H., Typke, D., Glaeser, R.M., and Jin, J. (2007). Design of a microfabricated, two-electrode phase-contrast element suitable for electron microscopy. Ultramicroscopy 107, 329–339.

Chang, W.H., Chiu, M.T., Chen, C.Y., Yen, C.F., Lin, Y.C., Weng, Y.P., Chang, J.C., Wu, Y.M., Cheng, H., Fu, J., and Tu, I.P. (2010). Zernike phase plate cryoelectron microscopy facilitates single particle analysis of unstained asymmetric protein complexes. Structure 18, 17–27.

Chen, D.H., Jakana, J., Liu, X., Schmid, M.F., and Chiu, W. (2008). Achievable resolution from images of biological specimens acquired from a 4k x 4k CCD camera in a 300-kV electron cryomicroscope. J. Struct. Biol. 163, 45–52.

Danev, R., Glaeser, R.M., and Nagayama, K. (2009). Practical factors affecting the performance of a thin-film phase plate for transmission electron microscopy. Ultramicroscopy 109, 312–325.

Danev, R., Kanamaru, S., Marko, M., and Nagayama, K. (2010). Zernike phase contrast cryo-electron tomography. J. Struct. Biol. 171, 174–181.

Danev, R., and Nagayama, K. (2008). Single particle analysis based on Zernike phase contrast transmission electron microscopy. J. Struct. Biol. 161, 211–218.

Dubochet, J., Adrian, M., Chang, J.J., Homo, J.C., Lepault, J., McDowall, A.W., and Schultz, P. (1988). Cryo-electron microscopy of vitrified specimens. Q. Rev. Biophys. 21, 129–228.

Faget, J., Fagot, M., Ferre, J., and Fert, C. (1962). Microscopie electronique a contraste de phase. In Proceedings of the 5th International Congress on Electron Microscopy. Abstract A-7. London, UK: Academic Press.

Gipson, B., Zeng, X., and Stahlberg, H. (2007a). 2dx_merge: data management and merging for 2D crystal images. J. Struct. Biol. 160, 375–384.

Gipson, B., Zeng, X., Zhang, Z.Y., and Stahlberg, H. (2007b). 2dx—user-friendly image processing for 2D crystals. J. Struct. Biol. 157, 64–72.

Glaeser, R.M., and Downing, K.H. (1990). The "specimen flatness" problem in high-resolution electron crystallography of biological macromolecules. In: Peachy, L.D. and Williams, D.B., eds. Proceedings of the XIIth International Congress for Electron Microscopy. Vol. 1. Seattle, WA: San Francisco Press, 98–99.

Hanszen, K.J. (1971). The optical transfer theory of the electron microscope: Fundamental principles and applications. In Advances in optical and electron microscopy, R. Barer and V.E. Cosslett, eds. (New York: Academic Press), pp. 1–84.

Henderson, R. (1995). The potential and limitations of neutrons, electrons and X-rays for atomic resolution microscopy of unstained biological molecules. Q. Rev. Biophys. 28, 171–193.

Henderson, R., Baldwin, J.M., Downing, K.H., Lepault, J., and Zemlin, F. (1986). Structure of purple membrane from Halobacterium halobium: recording measurement and evaluation of electron micrographs at 3.5 Å resolution. Ultramicroscopy 19, 147–178.

Hirai, T., Murata, K., Mitsuoka, K., Kimura, Y., and Fujiyoshi, Y. (1999). Trehalose embedding technique for high-resolution electron crystallography: application to structural study on bacteriorhodopsin. J. Electron Microsc. (Tokyo) 48, 653–658.

Jiang, W., Baker, M.L., Jakana, J., Weigele, P.R., King, J., and Chiu, W. (2008). Backbone structure of the infectious epsilon15 virus capsid revealed by electron cryomicroscopy. Nature 451, 1130–1134.

Jiang, W., Chang, J., Jakana, J., Weigele, P., King, J., and Chiu, W. (2006). Structure of epsilon15 bacteriophage reveals genome organization and DNA packaging/injection apparatus. Nature 439, 612–616.

Johnson, H.M., and Parsons, D.F. (1973). Enhanced contrast in electron microscopy of unstained biological material. 3. In-focus phase contrast of large objects. J. Microsc. 98, 1–17.

Kanaya, K., Kawakatsu, H., Ito, K., and Yotsumoto, H. (1958). Experiment on the electron phase microscope. J. Appl. Physiol. 29, 1046–1049.

Krakow, W., and Siegel, B.M. (1975). Phase contrast in electron microscope images with an electrostatic phase plate. Optik (Stuttg.) 44, 245–268.

Kremer, J.R., Mastronarde, D.N., and McIntosh, J.R. (1996). Computer visualization of three-dimensional image data using IMOD. J. Struct. Biol. 116, 71–76.

Liu, X., Jiang, W., Jakana, J., and Chiu, W. (2007). Averaging tens to hundreds of icosahedral particle images to resolve protein secondary structure elements using a Multi-Path Simulated Annealing optimization algorithm. J. Struct. Biol. 160, 11–27.

Liu, X., Zhang, Q., Murata, K., Baker, M.L., Sullivan, M.B., Fu, C., Dougherty, M.T., Schmid, M.F., Osburne, M.S., Chisholm, S.W., and Chiu, W. (2010a). Structural changes in a marine podovirus associated with release of its genome into prochlorococcus. Nat. Struct. Mol. Biol. 17, 830–836.

Liu, X., Rochat, R., and Chiu, W. (2010b). Reconstructing Cyano-bacterio-phage P-SSP7 structure without imposing symmetry. Nat. Protoc., published online. doi:10.1038/nprot.2010.96.

Ludtke, S.J., Baldwin, P.R., and Chiu, W. (1999). EMAN: semiautomated software for high-resolution single-particle reconstructions. J. Struct. Biol. 128, 82–97.

Majorovits, E., Barton, B., Schultheiss, K., Perez-Willard, F., Gerthsen, D., and Schroder, R.R. (2007). Optimizing phase contrast in transmission electron microscopy with an electrostatic (Boersch) phase plate. Ultramicroscopy 107, 213–226.

Mindell, J.A., and Grigorieff, N. (2003). Accurate determination of local defocus and specimen tilt in electron microscopy. J. Struct. Biol. 142, 334–347.

Nagayama, K. (2005). Phase contrast enhancement with phase plates in electron microscopy. Adv. Imaging Electron Phys. 138, 69–146.

Parsons, D., and Johnson, H.M. (1972). Possibility of a phase contrast electron microscope. Appl. Opt. 11, 2840–2843.

Pettersen, E.F., Goddard, T.D., Huang, C.C., Couch, G.S., Greenblatt, D.M., Meng, E.C., and Ferrin, T.E. (2004). UCSF Chimera—a visualization system for exploratory research and analysis. J. Comput. Chem. 25, 1605–1612.

Pintilie, G.D., Zhang, J., Goddard, T.D., Chiu, W., and Gossard, D.C. (2010). Quantitative analysis of cryo-EM density map segmentation by watershed and scale-space filtering, and fitting of structures by alignment to regions. J. Struct. Biol. *170*, 427–438.

Rosenthal, P.B., and Henderson, R. (2003). Optimal determination of particle orientation, absolute hand, and contrast loss in single-particle electron cryomicroscopy. J. Mol. Biol. *333*, 721–745.

Saad, A., Ludtke, S.J., Jakana, J., Rixon, F.J., Tsuruta, H., and Chiu, W. (2001). Fourier amplitude decay of electron cryomicroscopic images of single particles and effects on structure determination. J. Struct. Biol. *133*, 32–42.

Scherzer, O. (1949). The theoretical resolution limit of the electron microscope. J. Appl. Phys. *20*, 20–29.

Schmid, M.F., and Booth, C.R. (2008). Methods for aligning and for averaging 3D volumes with missing data. J. Struct. Biol. *161*, 243–248.

Schultheiss, K., Perez-Willard, F., Barton, B., Gerthsen, D., and Schroder, R.R. (2006). Fabrication of a Boersch phase plate for phase contrast imaging in a transmission electron microscope. Rev. Sci. Instrum. *77*, 033701.

Thon, F. (1971). Phase contrast electron microscopy. In Electron Microscopy in Material Sciences, U. Valdre, ed. (New York: Academic Press), pp. 571–625.

Toyoshima, C., and Unwin, N. (1988). Contrast transfer for frozen-hydrated specimens: determination from pairs of defocused images. Ultramicroscopy *25*, 279–291.

Unwin, P.N.T. (1970). An electrostatic phase plate for the electron microsope. Ber. Bunsenges Phys. Chem. *74*, 1137–1141.

Willasch, D. (1975). High resolution electron microscopy with profiled phase plates. Optik (Stuttg.) *44*, 17–36.

Yamaguchi, M., Danev, R., Nishiyama, K., Sugawara, K., and Nagayama, K. (2008). Zernike phase contrast electron microscopy of ice-embedded influenza A virus. J. Struct. Biol. *162*, 271–276.

Zernike, F. (1942). Phase contrast, a new method for the microscope observation of transparent objects. Physica *9*, 686–698.